THE OFFICIAL MAGAZINE OF THE OCEANOGRAPHY SOCIETY

Oceanography

CITATION

Jackson, C.R., J.C.B. da Silva, G. Jeans, W. Alpers, and M.J. Caruso. 2013. Nonlinear internal waves in synthetic aperture radar imagery. *Oceanography* 26(2):68–79, http://dx.doi.org/10.5670/oceanog.2013.32.

DOI

http://dx.doi.org/10.5670/oceanog.2013.32

Nonlinear Internal Waves in Synthetic Aperture Radar Imagery

BY CHRISTOPHER R. JACKSON, JOSÉ C.B. DA SILVA, GUS JEANS, WERNER ALPERS, AND MICHAEL J. CARUSO

ABSTRACT. Synthetic aperture radar (SAR) has contributed significantly to the study and understanding of oceanic nonlinear internal waves. Although they travel within the ocean's interior, currents associated with internal waves produce variations in ocean surface roughness that is readily detectable by SAR. This paper will first review the morphology of nonlinear internal wave signatures in SAR imagery and then examine the information that can be extracted from those signatures, including the determination of wave type and an estimation of phase speed.

A large internal solitary wave begins to impinge on Dongsha Atoll in the South China Sea in this Envisat ASAR image acquired on August 12, 2009, at 02:13:04 UTC. The incident wave refracts around the coral reef, resulting in a complex interaction pattern on its western side. Imaged area is approximately 125 km x 150 km.

INTRODUCTION

Oceanic nonlinear internal waves are oscillations that travel within the ocean along a pycnocline (i.e., a portion of the water column where the density changes maximally), typically the result of a sharp change in water temperature and/or salinity. This density change produces an interface along which nonlinear internal waves can propagate, similar to how the ocean surface (the interface between the atmosphere and ocean) supports the propagation of wind-driven waves. Internal waves have their origins in the barotropic tide (the tide that is caused by the astronomical forcing of the ocean) and can be generated in a variety of ways, including lee waves, tidal beams, resonance, plumes, and the transformation of the internal tide (Jackson et al., 2012). Nonlinear internal waves take the shape of a special waveform called a soliton, or solitary wave (see Zabusky and Porter, 2010), a class of nonsinusoidal waves of complex shape that has the ability to retain its form over extended periods of time.

Although they propagate along a pycnocline in the ocean's interior, currents within the nonlinear internal wave can produce convergent and divergent zones on the ocean surface that move in phase with the internal wave's subsurface crests and troughs. These zones have distinctive patterns of surface roughness that are readily detectable in both SAR and optical sunglint imagery. Many of the characteristic features of an internal wave's SAR signature can be found in Figure 1, a Seasat image acquired on September 29, 1978, over the Gulf of California. The internal wave signatures can be seen in groupings, or packets (labeled 1 through 8), of bright and/or dark curvilinear bands, with each band in a packet representing an individual internal solitary wave. As discussed in the following section, the SAR signatures of internal waves depend on a variety of factors related to the environmental conditions of both the surface and subsurface, as well as the properties of the internal wave itself. Several of the common signature morphologies are present in Figure 1, with light/dark band pair combinations or single dark bands visible against the gray background of the (undisturbed) sea surface as well as solitary wave interaction patterns (the dark "X" shaped features between packets 7 and 8).

In the Gulf of California, the packets originate from generation sites in the region south of San Lorenzo and San Esteban Islands (A in Figure 1) and between the island of Angle de la Guarda and the Baja Peninsula (B). Because the nonlinear internal waves remain coherent for up to several days, wave packets generated on several successive tidal cycles are visible in many SAR images. Newly generated packets are smaller in extent and contain fewer waves than more mature packets. As the packet propagates away from the generation site, additional waves within a packet are generated as the displaced pycnocline oscillates at the local Brunt-Väisälä period. (The Brunt-Väisälä, or buoyancy, period describes the oscillation of a water parcel about its equilibrium depth, and is used as a parameter to express the strength of stratification in a fluid). As the packet evolves, it expands front to back in the direction of propagation (because larger and faster waves are located at the leading edge of a packet) and also elongates in the along-crest direction.

The separation distance between packets (generated on successive tidal cycles at a common origin) can range from a few kilometers to more than 100 km, with the distance between leading waves in an individual packet ranging from a few tens of meters to tens of kilometers, with both depending on the phase speed of the waves and the time since generation. In situ observations show that the phase speeds of oceanic nonlinear internal waves can vary from less than 0.3 m s^{-1} to more than 3 m s^{-1}, with amplitudes (as measured as a displacement of the pycnocline) ranging from just a few meters to greater than 100 m.

Nonlinear internal waves occur globally with well-documented occurrences on the continental shelves, in straits, and in marginal seas (Farmer and Armi, 1988; Apel et al., 1985; Jackson, 2004). They provide an energy transfer mechanism between the large-scale tides and vertical mixing, often playing a key role

Christopher R. Jackson *(goa@internalwaveatlas.com) is Chief Scientist, Global Ocean Associates, Alexandria, VA, USA.* **José C.B. da Silva** *is Senior Scientist, Department of Geosciences, Environment and Spatial Planning and Centro Interdisciplinar de Investigação Marinha e Ambiental (CIIMAR), Universidade do Porto, Portugal.* **Gus Jeans** *is Director, Oceanalysis, Wallingford, UK.* **Werner Alpers** *is Professor Emeritus, Center for Marine and Atmospheric Sciences, Institute of Oceanography, University of Hamburg, Germany.* **Michael J. Caruso** *is Senior Systems Engineer, Center for Southeastern Tropical Advanced Remote Sensing, Rosenstiel School of Marine and Atmospheric Science, University of Miami, FL, USA.*

in biological primary production by affecting the exchange of heat, nutrients, and other properties between the shelf and the open ocean. They also represent a potential hazard to offshore operations (Hyder et al., 2005; see also Box 1).

This paper first reviews the morphology of nonlinear internal wave signatures in SAR imagery, imaging theories describing how the waves are detected in SAR, and factors that influence them. It then examines the types of information about internal wave properties that can be extracted from SAR signatures, including identifying internal wave type (depression, elevation) and mode, mapping out the geographic distribution of the wave occurrences, estimating their phase speed, and inferring information about the pycnocline and the upper ocean layer.

PROPERTIES OF INTERNAL WAVE SIGNATURES

Theory of SAR Imaging

In order for nonlinear internal waves to appear on SAR imagery, the internal wave must interact with the ocean surface and modify it at roughness scales that interact with the observing radar signal. As manifested on SAR images, a nonlinear internal wave packet typically appears as an alternating pattern of quasi-periodic bright and dark bands against a gray background. These radar bands result from enhanced and reduced radar backscatter, with the bright bands representing a convergence (rough) zone and the dark bands representing a divergent (smooth) zone. The convergence and divergence zones are the result of variations in the subsurface currents associated with the internal waves interacting with ocean surface. The most common pattern is a bright band followed by a dark band representing a nonlinear internal wave of depression (Figure 1, packets 1–6). However, a number of factors can affect the characteristics of this signature pattern, including the environment at the ocean surface (wind speed, wind direction, presence of surface films) and the properties of the internal wave itself (mode, half-width, amplitude, and currents).

Theoretical models describing the modulation of short-scale sea surface roughness by variable surface currents have been developed in the framework of weak hydrodynamic interaction theory (Alpers, 1985). When using this theory together with Bragg scattering theory,

Figure 1. A Seasat L-band synthetic aperture radar (SAR) image from the Gulf of California acquired September 29, 1978, at 18:11 UTC (Rev 1355). The image contains a variety of internal wave packet signatures, with the most prominent labeled 1–8. It shows many distinctive internal wave features: alternating bright/dark band signatures grouped into packets, packets from multiple tidal cycles present on a single image, and the nonlinear interaction between packets. The series of bright "dots" arrayed in a line across the image are the result of system calibration pulses (Fu and Holt, 1982). The imaged area is approximately 100 km x 270 km. *Seasat image courtesy of the Center for Southeastern Tropical Advanced Remote Sensing (CSTARS)*

which relates spectral values of the ocean surface waves to the normalized radar cross section (NRCS), the relationship between NRCS and surface current gradient $\frac{dU_x}{dx}$ can be written as:

$$\sigma = \sigma_0 (1 - A \frac{dU_x}{dx}), \quad (1)$$

where σ denotes the total NRCS, σ_0 is the NRCS of the background, x is the coordinate in the look direction of the SAR antenna projected onto the horizontal plane, and A is a constant that depends on radar wavelength, incidence angle, and relaxation rate. The relaxation rate is quite variable, depending on, among others things, wind speed and direction. The gradient $\frac{dU_x}{dx}$ is related to internal wave and upper ocean parameters such as amplitude and wavelength of the internal wave, as well as water column stratification. The larger the amplitude of the internal wave, the larger $\frac{dU_x}{dx}$ becomes. Equation 1 says that the NRCS becomes larger in convergent flow regions ($\frac{dU_x}{dx} < 0$) and smaller in divergent flow regions ($\frac{dU_x}{dx} > 0$), producing the bands of increased and decreased image intensity relative to a background. Other, more advanced, weak hydrodynamic interaction theories have been proposed (Romeiser and Alpers, 1997) and yield qualitatively similar results. In these theories, the variation of the NRCS or image intensity (also called the modulation depth) depends strongly on wind speed and direction (Brandt et al., 1999) and usually underestimates the strength of the variation because it does not include wave breaking. In addition, the theories require wind speeds to be above the threshold for Bragg wave generation (approximately 2–3 m s^{-1}) and below roughly 10 m s^{-1}, at which point the wind-generated roughness and the internal wave-generated roughness patterns can no longer be distinguished from each other.

There are also many instances where the internal wave's SAR signature appears only as a bright band on a gray (Figure 2) or black background (when the wind speed is below the Bragg generation threshold; see Figure 7A). Kudryavtsev et al. (2005) explain this morphology by accounting for specular reflection from breaking surface waves and Bragg scattering from short surface waves generated by wave breaking. Large solitary waves that propagate with speeds in excess of 2 m s^{-1} and have amplitudes > 50 m have surface roughness bands of sharply peaked meter-scale waves and white caps. The modulations induced by breaking events result in the bright-band-only signature. Similar bright band signatures are regularly observed with nearshore surface wave breaking.

Surface Films

The SAR signatures of internal waves, in addition to appearing in bright/dark band pairs (or as just a bright band), have also been observed as just dark bands against a gray background. This morphology is due to the presence of slicks on the ocean surface that interact

BOX 1. THE IMPACT OF INTERNAL WAVES ON OFFSHORE INDUSTRY

By Gus Jeans

Large-amplitude solitary internal waves cause strong, rapidly varying currents within the water column that are a proven hazard to offshore oil and gas developments in several regions of the world. These phenomena are now commonly referred to within the industry as solitons, following the pioneering work by Osborne et al. (1977). The authors describe the engineering impacts of the soliton's currents, which were responsible for a disruption to exploration drilling in the southern Andaman Sea. This industry experience led to the classic paper by Osborne and Burch (1980) that first linked soliton physics to oceanic nonlinear internal waves.

Soliton impact on exploration drilling has been noted in many other regions over recent decades, with key examples in Southeast Asia and offshore West Africa. Exploration drilling impacts include large tilts and horizontal displacements of rigs beyond the watch circle, excessive mooring line tensions, and overcompensation of dynamical positioning. Direct costs have included lost days of rig time and lost or damaged equipment. Additional risks to personnel and environment are more difficult to quantify. Beyond exploration, solitons have proven seriously disruptive to other offshore operations, including installation of drilling rigs, offloading from ships to drilling platforms, and vessel maneuvers. Hazards have been encountered offshore West Africa by various tandem vessels. The rapid onset of soliton currents has the potential to affect large floating structures in a similar way to squall winds. The impact of strong vertical motions to complex hybrid riser systems resulting from passing solitons remains poorly understood. Complex near-bed currents associated with internal wave breaking present a challenge to pipelines and other seabed infrastructure.

The continued need for an improved understanding of the risk posed by solitons prompted recent initiation of the Worldwide Internal Soliton Criteria project, described by Jeans et al. (2012). The application of SAR data has played a key role in the project, including an update of the established *Atlas of Internal Solitary-like Waves and Their Properties* (Jackson, 2004), drawing upon new material and a large commercial database of SAR images.

A passing internal solitary wave packet caused an oil rig to tilt. The tilt occurred even after prior warning permitted the rig to be properly secured. *Image provided courtesy of Fugro GEOS*

with the internal wave's currents and that are not considered within the hydrodynamic modulation and wave-breaking imaging theories. As early as 1950, Ewing (1950) recognized that internal waves could be detected at the sea surface by coherent slick bands that extended along the horizon for tens of kilometers with typical widths of the same scale as internal wave wavelengths (i.e., tens to hundreds of meters). Surface film slicks originate from surface active materials, or surfactants, particularly under low wind conditions. These smoothed areas are where the small gravity or capillary waves that make the surface look rough are missing or strongly attenuated. Indeed, anyone watching the ocean when winds are low may notice that some areas of the ocean surface appear smoother than adjacent areas. Surfactants are very effective in damping short wind waves. These surfactants may accumulate at the sea surface as a result of local current convergences, which enhance surfactant concentration and therefore bring together the organic molecules that compose a surface active film. Ermakov et al. (1992) were the first to comprehensively show how nonlinear internal waves accumulate surface films. Basically, currents in convergence zones at the sea surface act to enhance surfactant concentration (through accumulation), while currents in divergence zones reduce their influence (by tearing the films apart). The effect of wave damping by films varies nonlinearly with concentration.

Da Silva et al. (1998) showed that when surfactant films are present, they can modulate short-scale surface roughness so that the radar signature of an internal wave field consists of dark lines or bands only (areas of reduced radar backscatter) on a uniform gray background (as in Figure 3B). In simple terms, this change in signature character results from the competing effects of hydrodynamic modulation and surface films over the convergence zone of the internal wave. Film slicks eventually override the roughness generated at the surface convergence by hydrodynamic modulation, "eroding" the roughness bands and generating larger slick bands instead. In fact, da Silva et al. (2000) demonstrate the extent to which surface films may transform one type of signature into another. They show how an increase in background film concentration may trigger a transition from double-sign signatures (bright/dark bands) into single negative signatures (dark bands), all within a single internal solitary wave train. The combined effects of both mechanisms (hydrodynamic modulation and films) were synthesized in a film-pressure vs. wind speed diagram by these same authors (Figure 4). When SAR images of internal waves present bright and dark bands compared to the unmodulated background, the signature is classified as "double sign" (+/–). When the dark bands are wider and much more intense than the accompanying bright bands (which might even be absent from the image), this type of signature has been classified as "single negative sign" (–). When the internal waves appear as bright bands in a homogeneously dark (or dark-gray) background, the signature is classified as "single positive sign" (+). All of these signatures were quantitatively defined and studied by da Silva et al. (1998 and 2000).

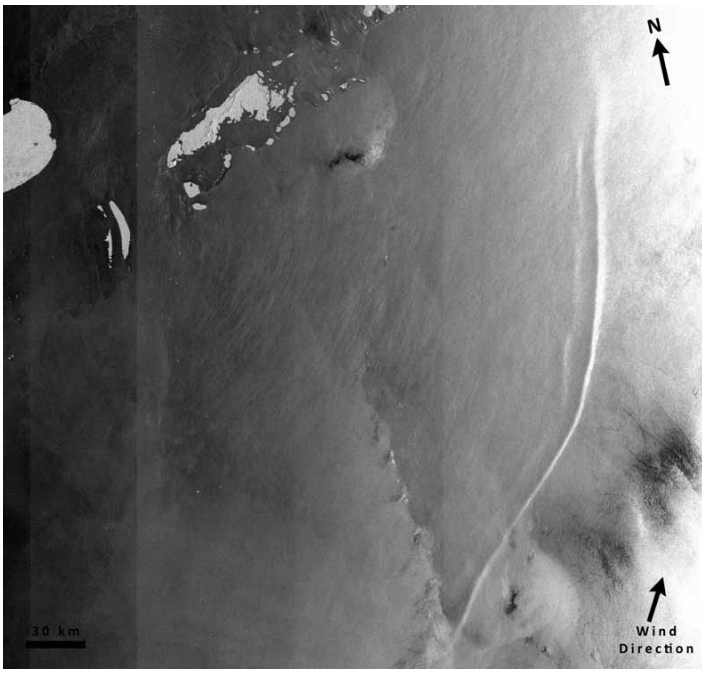

Figure 2. An Envisat C-band wide swath image of a large soliton in the Celebes Sea acquired on July 31, 2011, at 01:52 UTC. The image shows a large solitary wave signature as a bright band (relative to background). Wind speed is approximately 4.5 m s^{-1} around the wavefront and slightly higher (6.3 m s^{-1}) behind the wave near the center of the image.

INTERNAL WAVE PROPERTIES

With a better understanding of the properties associated with the SAR signatures of oceanic nonlinear internal waves, the next area to investigate is the information SAR imagery provides about the properties of internal waves. SAR imagery has been used to discriminate between internal waves of elevation and depression, map out the geographic distribution of the waves, identify generation regions, estimate the phase speed of the waves, and infer information about the pycnocline and the upper ocean layer.

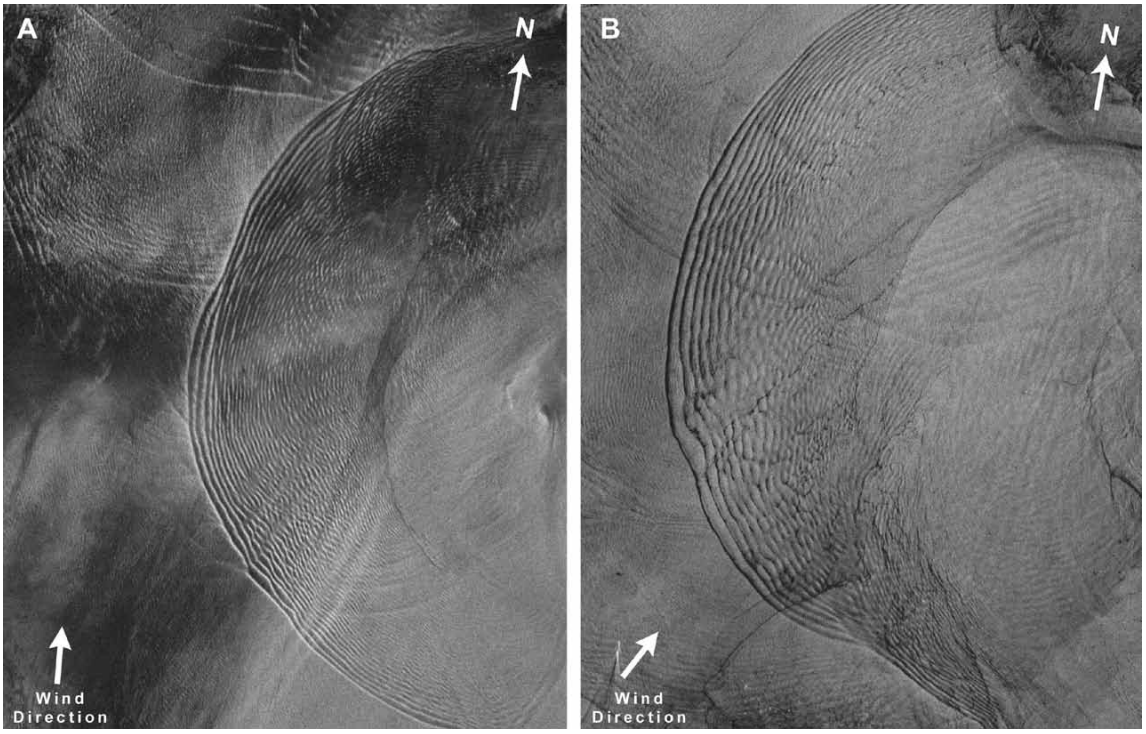

Figure 3. X-band SAR images acquired by TerraSAR-X over the Gulf of Maine west of Cape Cod on June 23, 2008, at 22:26 UTC (A) and July 3, 2008, at 22:26 (B). The images show the variability in the internal wave signature with the most common double-sign signatures in (A) (note the bright and dark bands compared with the local gray level) and a single negative signature (dark bands on a gray background) in (B). The wind speeds at the time of each image were 3.3 m s^{-1} (A) and 4.0 m s^{-1} (B).

Determination of Internal Wave Mode and Type

Up to this point, the discussion of signatures has focused on the most common manifestation of nonlinear internal waves in the ocean—the bright leading dark pattern of a mode-1 internal wave of depression. In this case, a single pycnocline divides the water column into an upper and a lower portion (a two-layer model). Internal wave physics dictates internal wave displacement into the thickest portion of the water column, typically the lower portion for most of the world ocean; hence, the situation consists of a single displacement (mode-1) toward the ocean bottom (depression). As discussed in the previous section, these waves most often have a bright enhanced backscatter feature preceding a dark reduced backscatter in the direction of wave propagation.

On the continental shelf, as the total water depth decreases toward shore, the upper layer (whose thickness may only change slightly) can occupy more than 50% of the stratified water column. In this situation, when a mode-1 depression wave propagates toward shore from deep water, solitons may first disintegrate into dispersive wave trains and then reorganize themselves as a packet of nonlinear waves of elevation after they pass through the turning point where the upper and lower layer thicknesses are approximately equal. With the reversal of the direction of displacement (now toward the surface) comes an associated reversal in the sequencing of the convergent and divergent zones. For waves of elevation, the SAR signature now consists of a dark reduced backscatter feature followed by a bright enhanced backscatter feature in the direction of wave propagation.

Liu et al. (1998) found evidence in European Remote Sensing satellite (ERS-1) SAR imagery of this transformation from depression to elevation waves (with the associated polarity change of the signature) off both Taiwan in the East China Sea and Hainan Island in the South China Sea. They simulated this evolution with a numerical model based

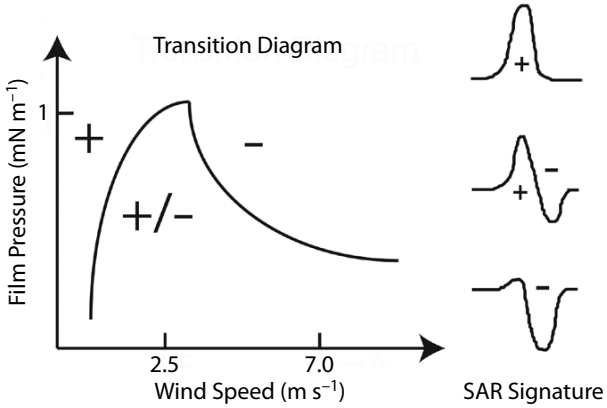

Figure 4. Internal wave diagram of signature modes derived from the European Remote Sensing Satellite (ERS) SAR. The different morphology of the internal wave SAR signature depends mainly on two parameters: film pressure and wind speed. The diagram should be regarded as qualitative in regard to the wind speed and film pressure values shown in the x and y axes, respectively (da Silva et al., 2000)

on the Kortewig-DeVries (KdV) equation. Robinson (2010) also presents an example of polarity change in the Gulf of Cadíz, off the Iberian Peninsula.

Different stratification conditions in the water column can support the existence of higher wave modes for internal waves. Mode-2 internal waves are characterized by the simultaneous rising of the upper pycnocline and lowering of the mid-pycnocline (a three-layer model) so that the wave travels as a bulge in the middle layer, displacing isopycnals upward into the upper layer and downward into the bottom layer (e.g., Shroyer, 2008). Mode-2 waves are waves of elevation, and with them come reversals in SAR signature polarity, with dark reduced backscatter crests preceding bright enhanced backscatter features in the direction of wave propagation.

Figure 5 presents a typical example of an internal solitary wave train with mode-2 structure, propagating toward the coast of Mozambique. The generation processes of mode-2 waves are still poorly understood (see Jackson, 2012). For the case shown in Figure 5, it is thought that a ray of internal tidal energy impinging on the thermocline from below is responsible for the generation of the mode-2 internal wave train (for more details see Mercier et al., 2012).

Because two distinct internal wave modes are capable of producing an identical dark/bright SAR signature pairing, additional information must be used to properly interpret modal structure. In general, a dark/bright signature in deep water is expected to belong to a mode-2 internal wave. Elevation waves can only exist when the upper layer depth is the thicker of the layers separated by the pycnocline, which is generally not the case for mode-1 waves in deep waters.

Internal Wave Occurrence Regions and Distribution

One of the primary uses of SAR in the study of internal waves has been to map out the geographic distribution of wave activity and help to identify the generation regions. The advent of larger area (multibeam position) data collection modes found on RADARSAT (ScanSAR) and Envisat (WideSwath) greatly enhanced this ability. With swath widths in excess of 400 km, internal wave observations could be made at basin-level scales. In Figure 6, a RADARSAT-1 image over the Andaman Sea shows how wide-swath-width imagery can provide information on multiple tidal cycles of internal wave activity and several days of wave packet evolution, important in understanding the activity in a region. With the ability to collect these kinds of data for more than a decade (from 1995 to 2013 for RADARSAT-1, 2002 to 2010

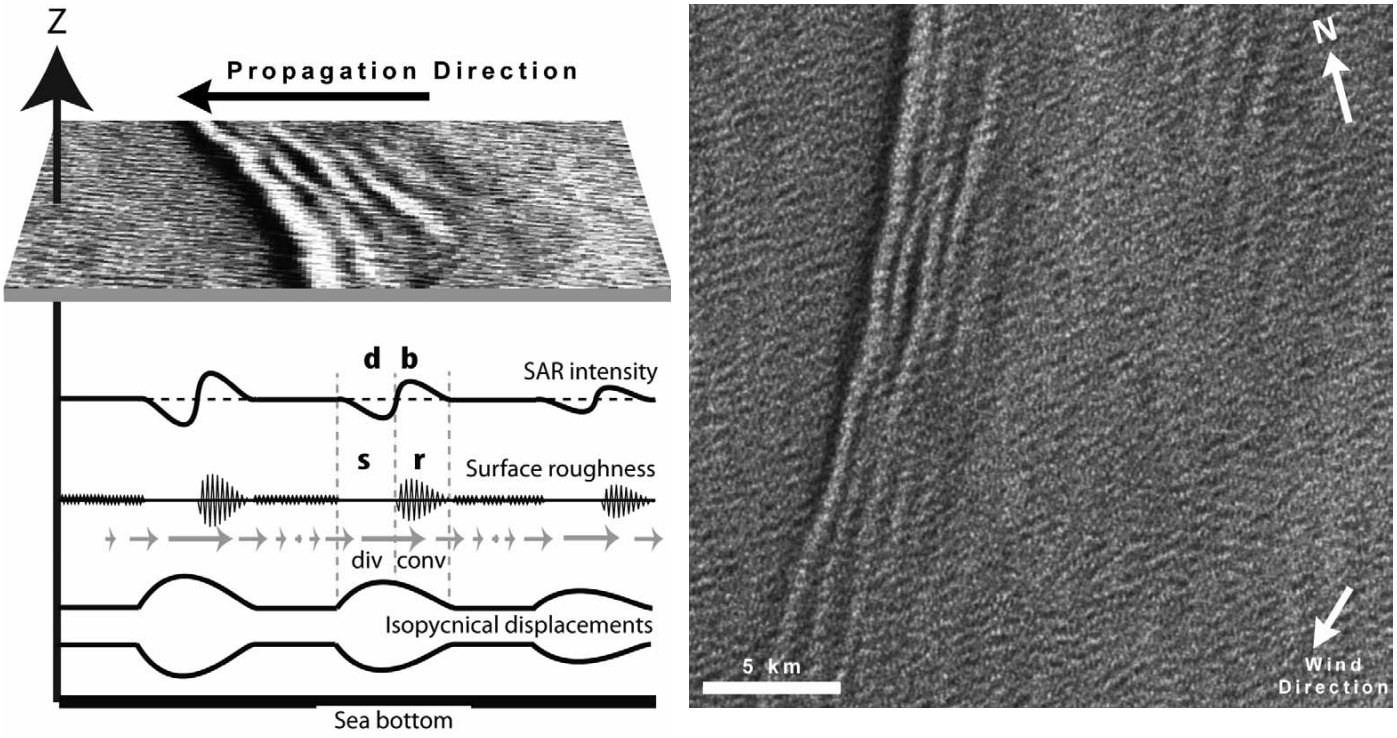

Figure 5. (left) Model scheme of the sea surface signature produced in a SAR image by a mode-2 internal solitary wave. (right) A full resolution ERS SAR image acquired September 24, 2001, at 07:39 UTC showing an internal wave signature in the Mozambique Channel consistent with mode-2 vertical structure. Wind speed was approximately 5.8 m s^{-1}. *Adapted from Mercier et al. (2012)*

for Envisat), there have been sufficient imaging opportunities to observe internal wave activity over all the continental shelves and the marginal seas.

Many researchers have used large amounts of SAR imagery to study the occurrence times and geographic distribution of internal waves. Dokken et al. (2001) studied internal wave activity along the coast of Norway using more than 2,600 ERS and RADARSAT-1 images. Liu et al. (1998), Hsu and Liu (2000), and Zhao et al. (2004) published maps showing the distribution of internal wave crest tracings for the South China Sea. Lorenzzetti and Dias (2013) identified over 460 internal solitary wave packets using 17 months of imagery from Envisat over the southeastern continental shelf of Brazil. These are only a few of the many studies that have been published. This ability to collect wide-swath imagery, which can show many tidal cycles worth of generated internal wave packets, is directly applicable to internal wave velocity estimation techniques.

Estimating Internal Wave Velocity

Typically, a given SAR image contains the signatures of several internal wave groups (or packets) with typical interpacket separations of the same order of magnitude as internal tidal waves (see Figures 1 and 6). The common assumption is that packet generation is associated with a specific time of the semidiurnal or diurnal tide because most internal wave generations result from interaction of barotropic tidal currents with bottom topography. This allows for a simple estimation of the average propagation speed from a single SAR image containing two packets with a common generation location. Their speed is determined by measuring the interpacket distance and dividing the result by the semidiurnal or diurnal tidal period, depending on the study region. Of course, this calculation only provides a rough estimate of the propagation speed because it is just an average over a relatively long time period. During that time, the propagation speed of the waves is subject to modification due to variable currents and/or vertical shears or very rapidly varying depth changes. In addition, wave generation may occur at slightly different phases of the tide due to interference between tidal constituents. Nevertheless, this type of estimation is easy to obtain and provides a good idea of the wave speeds in a given area.

A more precise measurement of internal wave packet propagation speed can be made based on multiple satellite images separated in time by less than a tidal period. This is now possible due to the number of satellite missions (both SAR and optical) with spatial resolutions capable of detecting internal solitary waves. However, satellite synergy pairs are dependent on satellite orbit matchups and this technique is restricted to appropriate image acquisition planning (or, more often, simply serendipitous image collections). Figure 7 shows two examples of such pairs from ERS-2 and Envisat. Figure 7A is from the northern portion of the South China Sea (northwest of Dongsha Atoll). Two large solitons visible in the images move approximately 3 km in the 31 minutes between the ERS and Envisat scenes, giving an internal wave velocity of 1.64 m s^{-1}. Figure 7B shows a similar translation between two different wave packets on the continental shelf off the east coast of the United States. In this case, the leading edges of the packets are found to move only 1.25 km (western packet) and 1.05 km (eastern packet) over 30 minutes, producing an internal wave velocity of 0.66 m s^{-1} and 0.53 m s^{-1}, respectively. This is significantly different than the 0.71 m s^{-1} estimate obtained from looking at the

Figure 6. RADARSAT-1 C-band ScanSAR Wide image from the Andaman Sea acquired on December 17, 1997, at 11:49 UTC. The image shows internal wave activity throughout the sea with more than two dozen internal wave packet signatures visible. The large number of internal wave sources in the southern portion of the sea results in overlapping packets and interaction signatures. The image shows how wide-swath imagery can provide information on multiple tidal cycles of internal wave activity and several days of wave packet evolution. Wind speed over the region is approximately 5 m s^{-1}. Imaged area is approximately 500 km x 1,000 km.

interpacket separation and assuming a 12.42-hour generation time difference.

When a number of images are available over the same region, it is possible to retrieve the propagation speed of internal wave packets in the region by assembling a travel-time graph. The travel-time graph technique relates a distance from a generation location point and a propagation time (defined as the time between the SAR image and a tidal reference time, for example, an extrema in the barotropic tidal flow) for the leading wave in an internal wave packet along a particular bearing. The times of tidal reference can be obtained from a tidal model such as OTIS/TPX06 (Egbert and Erofeeva, 2002), which should employ the relevant tidal constituents for a given region in a high-resolution model grid. The data points in a travel-time graph define the propagation of the internal waves through stratification and currents in a given bathymetry. Best-fit curves may be applied to these data points (e.g., see da Silva and Helfrich, 2008; da Silva et al., 2011), with the slopes of the curve producing an average propagation speed. In some cases, it is valid to assume that the internal solitary wave packets are trapped in the troughs of near-surface internal tides that are generated with a semidiurnal frequency (e.g., da Silva et al., 2011). Thus, the speeds derived from the slopes of the fitted curve are considered to represent the phase speeds of both the internal tides and the (leading) internal solitary wave in each packet. Scatter of the points about the idealized fit is to be expected as the waves may be refracted by varying stratification, propagate through variable currents and vertical shears, and originate at slightly different phases of the tide due to interference with diurnal constituents.

In estimating internal wave velocities in this manner, it is important to understand a limitation with observations from certain orbits. Remote-sensing satellites in sun-synchronous orbits, such as Envisat, allow images to be captured only at certain times of the semidiurnal tidal cycle. This is particularly evident in ocean regions where internal waves are mostly observed near spring tides, causing a kind of grouping of the data points (e.g., see Figure 5 in da Silva et al., 2011). Because the orbit is phase locked with the fortnightly spring-neap cycle, sampling within the flood-ebb cycle is

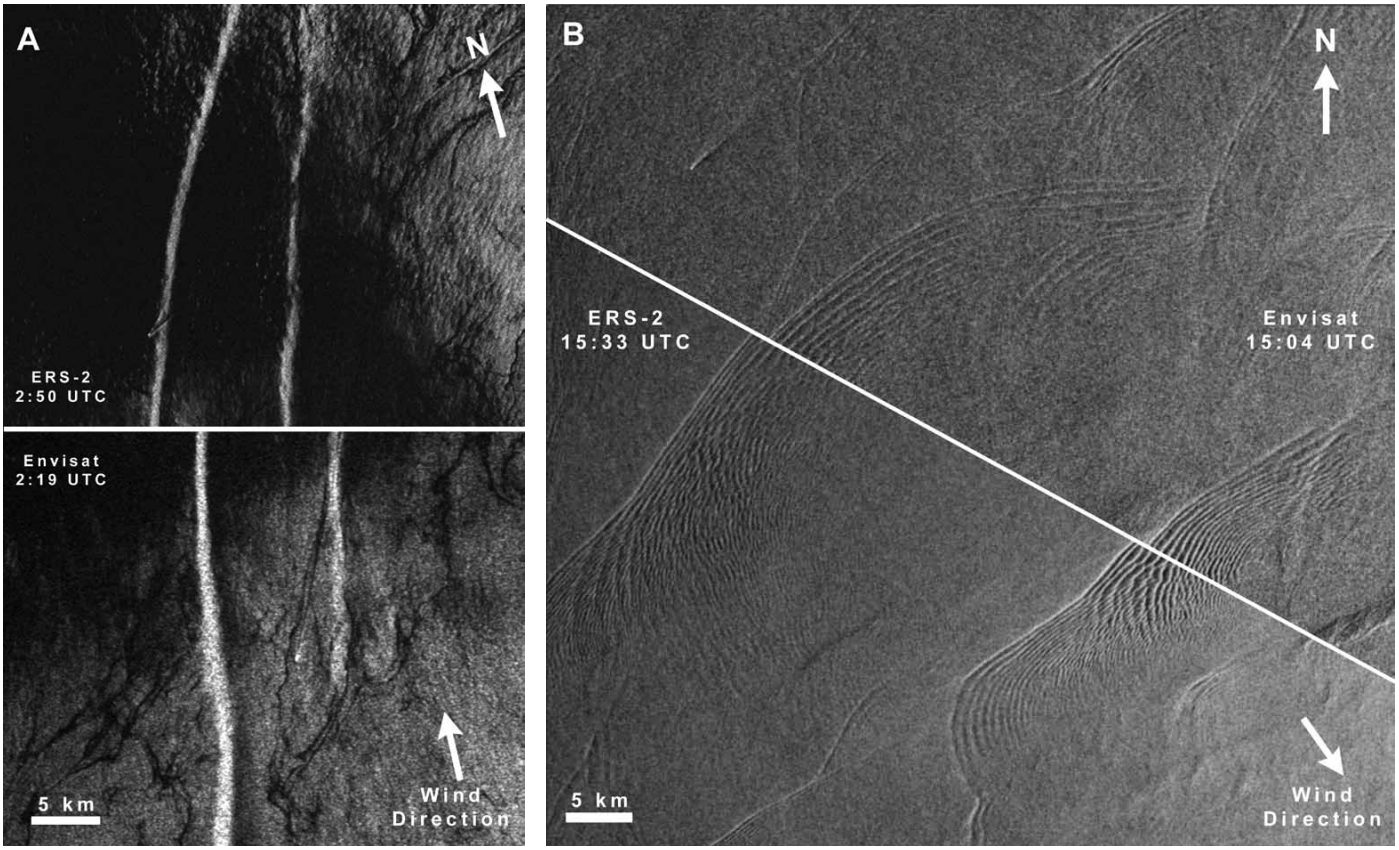

Figure 7. Two ERS-Envisat (C-band) image pairs showing the movement of internal waves. (A) Solitary waves in the South China Sea (near 20.6°N, 115.78°E) acquired on March 28, 2009, at 02:19 and 02:50 UTC. Wind speed is approximately 1.8 m s^{-1}. (B) Wave packets on the continental shelf along the east coast of the United States (near 39.5°N, 72.7°W) acquired August 8, 2006, at 15:04 and 15:33 UTC. Wind speed is approximately 6.4 m s^{-1}.

aliased so that the images always correspond to a similar flood-ebb phase of the semidiurnal tide.

Jackson (2009) developed a similar technique, but taking into account the locations of the leading internal wave at multiple bearings. The technique relies on a parameterized model function (relating internal wave phase speed to depth) to create a phase speed map that establishes a propagation time and propagation path between an origin and any location in the region of interest. Contours of propagation time (in longitude and latitude) represent the internal wave locations for a particular time since generation. The internal wave propagation time and propagation path can be calculated numerically by solving the two-dimensional eikonal differential equation with Fast Marching Methods (Sethian, 1999):

$$\left(\frac{\partial T(x, y)}{\partial x}\right)^2 + \left(\frac{\partial T(x, y)}{\partial y}\right)^2 = \frac{1}{C^2(x, y)}, \quad (2)$$

where $T(x, y)$ represents the travel time between an origin (x_0, y_0) and a location (x, y), and $C^2(x, y)$ is the parameterized velocity vs. depth function. The model parameters that dictate the wave speed are solved for minimizing the difference between the estimated propagation time and the observed propagation over the internal wave locations noted in the georeferenced imagery.

Ocean Environment: Mixed Layer Depth and Strength

Finally, with an accurate estimation of internal wave propagation speed, under certain conditions it is possible to estimate parameters of the upper ocean environment. Nonlinear internal wave theory shows (unsurprisingly) that there is a relationship between the properties of the nonlinear internal wave and the ocean environment through which it propagates. The relationship between the internal wave's propagation speed and the density structure of the water column offers the opportunity to use SAR internal wave observations to estimate the depth of the pycnocline and the density of the surface layer. The technique has been demonstrated using ERS-1 and RADARSAT-1 SAR imagery over the continental shelf off the east coast of the United States in summer (Porter and Thompson, 1999; Li et al., 2000), and in the Strait of Messina (Brandt et al., 1999). The authors relied on the dispersion relation, from a two-layer fluid model, which ties the propagation speed and the wavelength of the internal wave to the environmental parameters of water depth, pycnocline (or mixed layer) depth, and strength. With the internal wave parameters estimated from SAR imagery, the pycnocline depth and strength can be solved parametrically. A particular set of internal wave parameters may yield several mixed layer depth and strength combinations, and additional information is needed to determine the values uniquely.

The technique has several limitations that constrain where and when it can be used. First, internal waves must be present and detectable in the SAR imagery. In many areas, internal wave generation takes place during the days surrounding spring tides, ceasing generation around times of neap tide. The mixed layer needs to be present and strong enough to support internal wave generation and close enough to the surface for the internal wave to modulate surface roughness.

Nonlinear Interactions

The interaction effects between two solitary waves are significantly different from those of common "linear" waves. When two linear waves cross, the properties (phases, wavelength, or propagation direction) of the waves remain unchanged, while the combined amplitude is simply the sum (or linear combination) of the two individual wave amplitudes. However, when solitary waves cross, nonlinear interactions cause a phase shift in each of the individual waves, and the combined amplitudes can be up to four times the amplitude of an individual wave. The effects of the nonlinear interaction are dependent on the amplitude of the individual solitary waves and the angle at which the two waves cross (Wang and Pawlowicz, 2012). Different interaction angles produce different interaction patterns.

These nonlinear interaction patterns, which often resemble the shape of an "X" or a "Y," are readily detectable in SAR imagery, helping to show that oceanic internal waves exhibit solitary wave properties. Figure 8 shows an example of such a pattern for internal waves in the southern Andaman Sea. Here, two wave packets are crossing at approximately 135° and producing an "X"-type interaction. The interaction between the two leading solitons causes each to phase shift backward, and a connecting wave (called a Mach-stem) forms between them. The Mach stem brightness increases relative to the leading solitary wavefronts. Four additional enhanced brightness stems are visible as the different waves of the northern and southern packets interact. Figure 8 shows a particularly well-defined example of this interaction.

Miles (1977) undertook the first comprehensive investigation into such nonlinear interactions of internal waves. Kadomtsev and Petviashvili (1970) developed the theoretical basis for such interactions, and they extended the KdV equation into two dimensions. Wang and

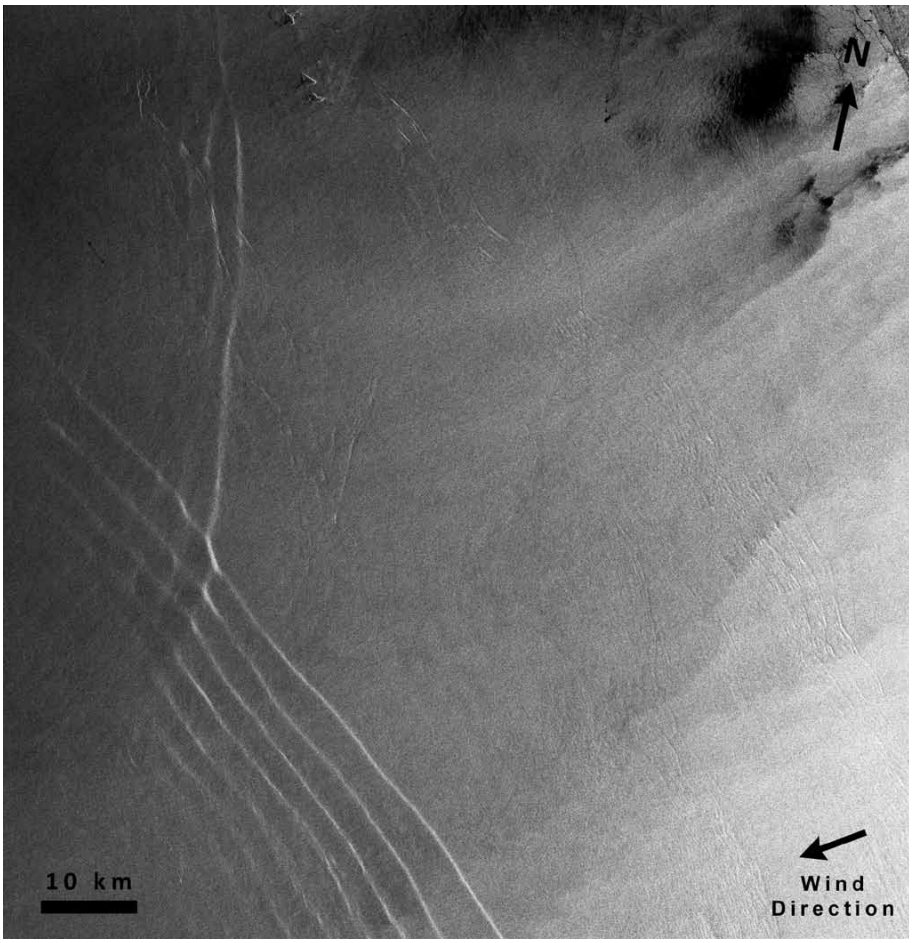

Figure 8. An Envisat (C-band) image from the Andaman Sea acquired November 18, 2006, at 18:20 UTC showing an "X" type soliton interaction pattern. The Mach-stem region connecting the waves shows enhanced surface brightness. Wind speed is approximately 8 m s^{-1}.

Pawlowicz (2012) present a more recent review of oblique angle solitary wave interactions, using the results in their interpretation of photographs of internal waves in the Strait of Georgia. In addition, Ablowitz and Baldwin (2012) show that these kinds of nonlinear interactions can be commonly observed among the small surface waves found along flat beaches at certain phases of the tide where the characteristics include wave breaking along the Mach-stems.

Finally, examining these kinds of nonlinear interactions could potentially provide valuable information about the relative amplitudes of solitons and the stem wave. These amplitude effects are of significant oceanographic interest because, in some cases, larger displacement can lead to breaking and, hence, enhanced mixing. In others, there may be a resonant transfer of energy between different waves, with implications for the propagation of energy and the effects of internal waves on offshore infrastructure such as oil platforms.

SUMMARY

SAR has been a key sensor for the study of oceanic nonlinear waves ever since Seasat showed their unique signatures over an unexpectedly widespread distribution of locations around the world. This paper presents an overview of the theories describing how internal waves are detected in SAR imagery and the factors that influence the morphology of their signatures. These factors include both surface and subsurface environmental conditions as well as the internal waves' properties. Individual wave signature manifestations include a light/dark band pair, a single dark band against a gray background, or a single light band against a gray or black background.

Patterns of these signatures provide a means of extracting information about an internal wave's properties, including determination of the type of wave (elevation/depression) and the wave mode (first or second). Phase shift patterns from soliton-soliton interactions confirm the nonlinear nature of the oceanic internal wave. The location of the signatures found in imagery permit mapping of the geographic distribution of wave occurrences and estimation of their phase speed (through a variety of techniques), which in turn can allow inferring information about the pycnocline and the thickness of the upper ocean layer.

ACKNOWLEDGEMENTS

C.J. gratefully acknowledges the support of the Office of Naval Research through contract N0001409C0224, the European Space Agency for providing imagery under Cat-1 Project 2746, and CSTARS for providing the Seasat imagery. J.C.B. da Silva's research was partially supported by the project PEst-C/MAR/LA0015/2011 funded by Fundacao para a Ciencia e a Tecnologia and the European Regional Development Fund through the COMPETE—Operational Competitiveness Programme as part of the National Strategic Reference Framework. TerraSAR-X imagery was acquired from The German Aerospace Centre (DLR) under the project OCE0056.

REFERENCES

Ablowitz, M.J., and D.E. Baldwin. 2012. Nonlinear shallow ocean-wave soliton interactions on flat beaches. *Physical Review E* 86(3), 036305, http://dx.doi.org/10.1103/PhysRevE.86.036305.

Alpers, W. 1985. Theory of radar imaging of internal waves. *Nature* 314:245–247, http://dx.doi.org/10.1038/314245a0.

Apel, J.R., J.R. Holbrook, A.K. Liu, and J.J. Tsai. 1985. The Sulu Sea internal soliton experiment. *Journal of Physical Oceanography* 15(12):1,625–1,651, http://dx.doi.org/10.1175/1520-0485(1985)015<1625:TSSISE>2.0.CO;2.

Brandt, P., R. Romeiser, and A. Rubino. 1999. On the determination of characteristics of the interior ocean dynamics from radar signatures of internal solitary waves. *Journal of Geophysical Research* 104(C12):30,039–30,045, http://dx.doi.org/10.1029/1999JC900092.

da Silva, J.C.B., S.A. Ermakov, and I.S. Robinson. 2000. Role of surface films in ERS SAR signatures of internal waves on the shelf: 3. Mode transitions. *Journal of Geophysical Research* 105(C10):24,089–24,104, http://dx.doi.org/10.1029/2000JC900053.

da Silva, J.C.B., S.A. Ermakov, I.S. Robinson, D.R.G. Jeans, and S.V. Kijashko. 1998. Role of surface films in ERS SAR signatures of internal waves on the shelf: 1. Short-period internal waves. *Journal of Geophysical Research* 103(C4):8,009–8,031, http://dx.doi.org/10.1029/97JC02725.

da Silva, J.C.B., and K.R. Helfrich. 2008. Synthetic aperture radar observations of resonantly generated internal solitary waves at Race Point Channel (Cape Cod). *Journal of Geophysical Research* 113, C11016, http://dx.doi.org/10.1029/2008JC005004.

da Silva, J.C.B., A.L. New, and J.M. Magalhaes. 2011. On the structure and propagation of internal solitary waves generated at the Mascarene Plateau in the Indian Ocean. *Deep Sea Research Part I* 58:229–240, http://dx.doi.org/10.1016/j.dsr.2010.12.003.

Dokken, S.T., R. Olsen, T. Wahl, and M.V. Tantillo. 2001. Identification and characterization of internal waves in SAR images along the coast of Norway. *Geophysical Research Letters* 28:2,803–2,806, http://dx.doi.org/10.1029/2000GL012730.

Egbert, G.D., and S.Y. Erofeeva. 2002. Efficient inverse modeling of barotropic ocean tides. *Journal of Atmospheric and Oceanic Technology* 19:183–204, http://dx.doi.org/10.1175/1520-0426(2002)019<0183:EIMOBO>2.0.CO;2.

Ermakov, S.A., S.G. Salashin, and A.R. Panchenko. 1992. Film slicks on the sea surface and some mechanisms of their formation. *Dynamics of Atmospheres and Oceans* 16(3):279–304, http://dx.doi.org/10.1016/0377-0265(92)90010-Q.

Ewing, G. 1950. Slicks, surface films and internal waves. *Journal of Marine Research* 9:167–187.

Farmer, D.M., and L. Armi. 1988. The flow of Mediterranean Water through the Strait of Gibraltar, the flow of Atlantic water through the Strait of Gibraltar. *Progress in Oceanography* 2:1–105, http://dx.doi.org/10.1016/0079-6611(88)90055-9.

Fu, L.L., and B. Holt. 1982. *Seasat Views Oceans and Sea Ice With Synthetic Aperture Radar*. JPL Publication 81-120, National Aeronautics and Space Administration, Jet Propulsion Laboratory, Pasadena, CA, 204 pp. Available online at: http://southport.jpl.nasa.gov/reports/seasat/seasat.pdf (accessed July 16, 2013).

Hsu, M.K., and A.K. Liu. 2000. Nonlinear internal waves in the South China Sea. *Canadian Journal of Remote Sensing* 26:72–81.

Hyder, P., D.R.G. Jeans, E. Cauquil, and R. Nerzic. 2005. Observations and predictability of internal solitons in the Northern Andaman Sea. *Journal of Applied Ocean Research* 27:1–11, http://dx.doi.org/10.1016/j.apor.2005.07.001.

Jackson, C.R. 2004. *An Atlas of Internal Solitary-like Waves and Their Properties*, 2nd ed. Global Ocean Associates, Alexandria, VA, 560 pp. Available online at: http://www.internalwaveatlas.com (accessed July 16, 2013).

Jackson, C.R. 2009. An empirical model for estimating the geographic location of nonlinear internal solitary waves. *Journal of Atmospheric and Oceanic Technology* 26:2,243–2,255, http://dx.doi.org/10.1175/2009JTECHO638.1.

Jackson, C.R., J.C.B. da Silva, and G. Jeans. 2012. The generation of nonlinear internal waves. *Oceanography* 25(2):108–123, http://dx.doi.org/10.5670/oceanog.2012.46.

Jeans, G., M. Calverley, W. Jeffery, C. Jackson, V. Vlasenko, and A.R. Osborne. 2012. Worldwide internal soliton criteria. Paper presented at Oceanology International 2012, London, UK, March 14–15, 2012.

Kadomtsev, B.B., and V.I. Petviashvili. 1970. On the stability of solitary waves in weakly dispersive media. *Soviet Physics, Doklady* 15:539–541.

Kudryavtsev, V., D. Akimov, J.A. Johannessen, and B. Chapron. 2005. On radar imaging of current features: 1. Model and comparison with observations. *Journal of Geophysical Research* 110, C07016, http://dx.doi.org/10.1029/2004JC002505.

Li, X., P. Clemente-Colon, and K.S. Friedman. 2000. Estimating oceanic mixed-layer depth from internal wave evolution observed from RADARSAT-1 SAR. *Johns Hopkins APL Technology Digest* 21:130–135.

Liu, A.K., Y.S. Chang, M.-K. Hsu, and N.K. Liang. 1998. Evolution of nonlinear internal waves in the East and South China Seas. *Journal of Geophysical Research* 103(C4):7,995–8,008, http://dx.doi.org/10.1029/97JC01918.

Lorenzzetti, J.A., and F.G. Dias. 2013. Internal solitary waves in the Brazilian SE continental shelf: Observations by synthetic aperture radar. *International Journal of Oceanography* 2013, 403259, http://dx.doi.org/10.1155/2013/403259.

Mercier, M.J., M. Mathur, L. Gostiaux, T. Gerkema, J.M. Magalhães, J.C. da Silva, and T. Dauxois. 2012. Soliton generation by internal tidal beams impinging on a pycnocline: Laboratory experiments. *Journal of Fluid Mechanics* 704:37–60, http://dx.doi.org/10.1017/jfm.2012.191.

Miles, J.W. 1977. Obliquely interacting solitary waves. *Journal of Fluid Mechanics* 79:157–169, http://dx.doi.org/10.1017/S0022112077000081.

Osborne, A.R., J.R. Brown, T.L. Burch, and R.I. Scarlet. 1977. The influence of internal waves on deepwater drilling operations. Paper presented at the Offshore Technology Conference, May 2–5, 1977, Houston, TX.

Osborne, A.R., and T.L. Burch. 1980. Internal solitons in the Andaman Sea. *Science* 208:451–460, http://dx.doi.org/10.1126/science.208.4443.451.

Porter, D.L., and D.R. Thompson. 1999. Continental shelf parameters inferred from SAR internal wave observations. *Journal of Atmospheric and Oceanic Technology* 16:475–487, http://dx.doi.org/10.1175/1520-0426(1999)016<0475:CSPIFS>2.0.CO;2.

Robinson, I.S. 2010. *Discovering the Ocean from Space: The Unique Applications of Satellite Oceanography*. Springer, 638 pp.

Romeiser, R., and W. Alpers. 1997. An improved composite surface model for the radar backscattering cross section of the ocean surface: Part 2. Model response to surface roughness variations and the radar imaging of underwater bottom topography. *Journal of Geophysical Research* 102(C11):25,251–25,267, http://dx.doi.org/10.1029/97JC00191.

Sethian, J.A. 1999. *Level Set Methods and Fast Marching Methods: Evolving Interfaces in Computational Geometry, Fluid Mechanics, Computer Vision, and Materials Science*, 2nd ed. Cambridge University Press, 378 pp.

Shroyer, E. 2008. Varicose waves. (Box in Small-scale processes in the coastal ocean by J.N. Moum, J.D. Nash, and J.M. Klymak.) *Oceanography* 21(4):28, http://dx.doi.org/10.5670/oceanog.2008.02.

Wang, C., and R. Pawlowicz. 2012. Oblique wave-wave interactions of nonlinear near-surface internal waves in the Strait of Georgia. *Journal of Geophysical Research* 117, C06031, http://dx.doi.org/10.1029/2012JC008022.

Zabusky, N.J., and M.A. Porter. 2010. Soliton. *Scholarpedia* 5(8):2068, http://dx.doi.org/10.4249/scholarpedia.2068.

Zhao, Z., V. Klemas, Q. Zheng, and X.-H. Yan. 2004. Remote sensing evidence for baroclinic tide origin of internal waves in the northeastern South China Sea. *Geophysical Research Letters* 31, L06302, http://dx.doi.org/10.1029/2003GL019077.